Dalton Transactions

Accepted Manuscript

ROYAL SOCIETY OF CHEMISTRY

www.rsc.org/dalton

Remarkably enhanced photocatalytic activity of ordered mesoporous carbon/g-C_3N_4 composites photocatalyst under visible light

Lei Shi [b], Lin Liang [a, c], Jun Ma [a], Fangxiao Wang [b], Jianmin Sun [a, b*]

a: State Key Laboratory of Urban Water Resource and Environment, Harbin Institute of Technology, Harbin 150080, China

b: The Academy of Fundamental and Interdisciplinary Science, Harbin Institute of Technology, Harbin 150080, China

c: School of Life Science and Technology, Harbin Institute of Technology, Harbin 150080, China

*Corresponding author. Tel: +86 451 86403715;

E-mail address: sunjm@hit.edu.cn

Abstract

Ordered mesoporous carbon/g-C_3N_4 (OMC/g-C_3N_4) composites with efficient photocatalytic activity under visible light irradiation were prepared by a facile heating method. The as-prepared OMC/g-C_3N_4 composites were thoroughly characterized by X-ray diffraction, Fourier transform infrared spectroscopy, elemental analyses, transmission electron microscopy with energy dispersion X-ray spectrum, N_2 adsorption–desorption isotherms, UV-vis diffuse reflectance spectra and photoluminescence spectra. The photocatalytic activities were evaluated by degrading Rhodamine B dye and OMC/g-C_3N_4 composites exhibited much higher photocatalytic activities than pristine g-C_3N_4. Moreover, the catalysts kept good stability and the photodegradation efficiency hardly changed after five recycles. The degradation rate of OMC/g-C_3N_4 photocatalyst was almost 10 times as high as that of the pristine g-C_3N_4, which indicated that OMC played an important role in remarkably improved photocatalytic activity. The significant enhancement in photodegradation activity over OMC/g-C_3N_4 catalyst could be ascribed to the combined effects coming from the enhanced visible light adsorption, enriched adsorption of dye on the catalyst and subsequent efficient separation of photogenerated electrons and holes. In addition, a possible mechanism for the photodegradation process was proposed on the basis of active species scavenging experiments.

Keywords: OMC/g-C_3N_4 composite, photocatalyst, visible light, RhB dye

1. Introduction

Semiconductor photocatalysis has attracted tremendous attention due to its wide applications for hydrogen production from splitting water and degradation of environmental pollutants. [1-6] For large-scale application, an ideal photocatalyst should possess the advantages such as low price, availability and stability, and would work efficiently under visible light to utilize the main components of the solar spectrum. Of the special interest, TiO_2 was the most widely studied material due to its high activity, stability, low cost and non-toxicity. [7-10] However, the large band gap 3.2 eV of TiO_2 seriously limited its utilization of the solar spectrum. Hence, the discovery of the novel photocatalyst with high activity under visible light illumination is highly desirable.

Recently, as a promising metal-free photocatalyst, graphitic carbon nitride (g-C_3N_4) has drawn great interests owing to its non-toxicity, abundance and stability. [11-13] g-C_3N_4 with narrow band gap of 2.7 eV exhibited good photocatalytic performance for water splitting and degradation of organic pollutants. [14-25] Although g-C_3N_4 has been explored as a promising candidate photocatalyst, the high recombination rate of its photogenerated electron-hole pairs, the absorbance of only blue light up to 460 nm and low specific surface area restricted utilization of solar energy, leading to poor efficiency in photocatalytic reactions. How to overcome the problems has become the challenge. Consequently, some strategies such as nonmetal doping, [26] metal doping, [27] conjugated polymer modification, [28] coupling with semiconductors composite, [29] and anchoring dye sensitization, [30] have been developed.

And another feasible route to improve the quantum efficiency is to promote the separation efficiency of photogenerated electron-hole pairs.

It has been found that carbon modified semiconductors can accelerate electron transfer from photocatalyst to the liquid-solid interface by taking advantage of carbon's unique electron transport ability. [31-35] g-C_3N_4 coupled with carbonaceous materials to enhance the photocatalytic activity have been reported. Xiang et al. synthesized the graphene/C_3N_4 composites by the impregnation-chemical reduction strategy. The as-made composites possessed an improved photocatalytic hydrogen production rate under visible light irradiation. [36] Ge et al. prepared multi-wall carbon nanotubes/C_3N_4 composites, which exhibited high visible light photocatalytic activity for hydrogen production. [37] Liao et al. fabricated the graphene oxide modified C_3N_4 by sonochemical approach and the photocatalytic degradation rate constants of Rhodamine B (RhB) and 2,4-dichlorophenol with GO/C_3N_4 under visible light irradiation were 3.80 and 2.08 times larger than those with pristine C_3N_4. [38] Ordered mesoporous carbon, which possess tubular structure and large pore sizes, high surface areas, periodically arranged monodispersed mesopore space provide a good opportunity for composite with photocatalyst. The combination of ordered mesoporous carbon with g-C_3N_4 may be a promising efficient photocatalyst. However, to the best of our knowledge, there are no reports on the photocatalytic material composed of ordered mesoporous carbon and g-C_3N_4 for the contaminate degradation. In this paper, the novel ordered mesoporous carbon/g-C_3N_4 (OMC/g-C_3N_4) composites were facilely synthesized and their composition, morphology and optical

properties were well characterized. Moreover, the photocatalytic activity and stability of the composites were evaluated for degrading dye RhB under visible light, furthermore, the possible mechanism for dye degradation was proposed based on the present experimental results.

2. Experimental

2.1 Materials synthesis

2.1.1 Fabrication of C/SBA-15

Firstly, SBA-15 was prepared as the literature work. [39] 2 g Pluronic P123 ($EO_{20}PO_{70}EO_{20}$, Mw ~5800) was dissolved into 75 g of 1.6 M HCl at 40 °C for overnight. 4.25 g tetraethylorthosilicate (TEOS) was added to the above transparent solution and the mixture was stirred for 24 h. Then the mixture was subsequently treated at 100 °C for another 24 h in an autoclave. The as-prepared SBA-15 was collected by filtration, washed by distilled water twice, dried at 80 °C for overnight and finally calcined at 500 °C for 6 h in the air to get the final product. And the detailed characterization for SBA-15 was provided in supporting information.

1 g as-prepared SBA-15 powder was dispersed into the mixture solution containing 1.25 g sucrose and 0.14 g H_2SO_4 (98%) in 5 g water and stirred for 12 h at room temperature. The mixture was heated at 100 °C for 6 h and subsequently at 160 °C for another 6 h in the air. The impregnation process was repeated once with another solution containing 0.8 g sucrose and 5 g water containing 0.09 g H_2SO_4 (98%). The dark brown composites were completely carbonized at 900 °C for 5 h in

N_2 atmosphere at a heating rate of 2 °C min^{-1} to obtain carbon coated SBA-15, denoted as C/SBA-15.

2.1.2 Synthesis of OMC/g-C_3N_4

The specified amounts of C/SBA-15 and 3 g melamine were dispersed into 20 mL distilled water under stirring for 2 h. The mixture was dried at 50 °C for 5 h under stirring, then placed in a crucible with a cover. The crucible was heated to 500 °C for 2 h and 520 °C for 2 h at a heating rate of 4 °C min^{-1}. Then the crucible was cooled to room temperature. The as-prepared composites were stirred in 10% hydrofluoric acid for 24 h, then collected by filtration, washed by water and finally dried at 80 °C for 12 h. The obtained samples were denoted as OMC/g-C_3N_4-1, OMC/g-C_3N_4-2 and OMC/g-C_3N_4-3 with 0.05 g, 0.10 g and 0.20 g C/SBA-15 added, respectively.

2.2 Material characterizations

The patterns of small-angle X-ray diffraction (SAXRD, 0.6–5°) and wide-angle X-ray diffraction (WAXRD, 10–80°) were carried out on Bruker D8 Advance X-ray powder diffractometer with Cu Kα radiation (40 kV, 40 mA) for phase identification. Fourier transform infrared spectroscopy (FTIR) was recorded in transmission mode from 4000 to 400 cm^{-1} on a Perkin Elmer spectrum 100 FTIR spectrometer using KBr discs. Elemental analyses (EA) for the carbon and nitrogen contents were performed on Vario Microcube CHN analyzer. The morphology and particle size of the sample supporting on copper mesh were examined by transmission electron microscopy (TEM, Tecnai G2 Spirit) equipped with an energy dispersion X-ray spectrum (EDS). N_2 adsorption–desorption isotherms were collected at 77 K using a Quantachrome

NOVA 2000 surface area and porosity analyzer. Samples were outgassed at 150 °C for 12 h prior to measurements. The UV-vis diffuse reflectance spectra (DRS) were measured by a Perkin Elmer Lambda 750 UV/vis spectrometer. The photoluminescence spectra (PL) were obtained by a Varian Cary Eclipse spectrometer with an excitation wavelength of 325 nm.

2.3 Photocatalytic testing

The photocatalytic performance of OMC/g-C_3N_4 composites was evaluated through degrading RhB dye under visible light. A 300 W Xe lamp with a 420 nm cutoff filter was used as the light source to provide visible light irradiation. 50 mg OMC/g-C_3N_4 composites were dispersed into 100 mL 5 mg L^{-1} RhB solution for photocatalytic examinations under magnetic stirring. Prior to the light irradiation, the dispersion was kept in dark for 60 min under magnetic stirring to reach the adsorption-desorption equilibrium. Solutions were collected every 15 min and centrifuged to remove the catalyst then analyzed on UV-vis spectrometer. For comparison, the reactions were carried out in the presence of pure g-C_3N_4 powder and in the absence of any catalyst. The efficiency of degradation was calculated by C/C_0, wherein C is the concentration of remaining dye solution at each irradiated time, and C_0 is the initial concentration.

2.4 The stability of catalyst

The stability of OMC/g-C_3N_4 composite under visible light irradiation was investigated by recycling experiment. After the photodegradation of RhB, the separated photocatalyst was washed with water and ethanol for several times, dried at

80 °C for 12 h, then applied to degrade a fresh 5 mg L^{-1} RhB aqueous solution under the same conditions for another run. The recycling process was repeated up to 5 times.

2.5 Determination of reactive species.

To detect the active species generated in the photocatalytic process, various scavengers including methanol (10 mmol L^{-1}), p-benzoquinone (p-BQ, 1 mmol L^{-1}), dimethyl sulfoxide (DMSO, 5 mmol L^{-1}) and ammonium oxalate (AO, 1 mmol L^{-1}) were introduced into the solution of RhB. The other photocatalytic process was the same as the part 2.3.

3. Results and Discussion

XRD patterns of the pure g-C_3N_4 and OMC/g-C_3N_4 composites were shown in Figure 1. The OMC displayed a very broad diffraction peak at around 23°. All the OMC/g-C_3N_4 composites had similar diffraction peaks with pristine g-C_3N_4. The strong one at 27.4° indicated the graphite-like stacking of the conjugated aromatic units of CN, which was indexed to (002) plane of hexagonal g-C_3N_4 (JCPDS card no. 87-1526), corresponding to the interplanar distance of 0.325 nm. The other diffraction peak at 13.1° was assigned to (100) plane, which was associated with interlayer stacking, corresponding to the interplanar distance of 0.675 nm. [19, 24] Inset is the SAXRD patterns of OMC and OMC/g-C_3N_4 composites. The obvious one peak at 1.2° and another small peak at 1.9° in OMC sample suggested the existence of periodical mesopores. However, due to the low amounts of OMC and its high dispersion in composites, the peak intensities at 1.2° in OMC/g-C_3N_4-2 and OMC/g-C_3N_4-3

composites decreased significantly and the other peaks at 1.9° were unobvious. In the case of OMC/g-C_3N_4-1 composite, the SAXRD peak was almost undetected with OMC amount further decreasing.

(Figure 1)

Figure 2 showed the FTIR spectra of pure g-C_3N_4, OMC and a series of OMC/g-C_3N_4 composites. Pure g-C_3N_4 displayed peaks at 806 cm^{-1}, 1248 cm^{-1}, 1323 cm^{-1}, 1414 cm^{-1}, 1456 cm^{-1}, 1566 cm^{-1} and 1635 cm^{-1}. The absorption peak at 806 cm^{-1} was attributed to the out-of-plane skeletal bending modes of the triazine cycles, [28] and the absorption bands in the range of 1200-1700 cm^{-1} were assigned to the typical stretching modes of CN heterocycles. [19] The broad band in the range of the 3000-3500 cm^{-1} region was attributed to the adsorbed O-H bands and N-H components, [15] which suggested that the amino groups were not removed thoroughly during the pyrolysis process of melamine. The residual hydrogen atoms bonded to the edges of the graphene-like C-N sheet in the form of C-NH_2 and 2C-NH bonds. Similar phenomenon was reported in the previous work.[19, 36, 40] For the pristine OMC, the FTIR spectrum was a smooth curve and no strong stretching vibration peaks were found. And in the case of OMC/g-C_3N_4 composites, the low loaded amounts of OMC led to the undetected FTIR spectroscopy.

(Figure 2)

To demonstrate the different element contents in the OMC/g-C_3N_4 composites, elemental analyses of pure g-C_3N_4 and OMC/g-C_3N_4 were listed in Table 1. The atomic ratio of carbon to nitrogen in pure g-C_3N_4 was 0.65. And the atomic ratios of

carbon to nitrogen in OMC/g-C_3N_4-1, OMC/g-C_3N_4-2 and OMC/g-C_3N_4-3 were improved to 0.68, 0.74 and 0.79, respectively, which were resulted from the additions of OMC.

(Table 1)

The morphology and microstructure of the pure g-C_3N_4 and OMC/g-C_3N_4-2 were investigated by TEM. As seen from Figure 3A, pure g-C_3N_4 consisted of irregular shapes with aggregated structures. Figure 3B-C displayed the obvious OMC existence with an assembly of hexagonal arrays separated by 2-3 nm channel voids, which was agreement with XRD result. In the case of OMC/g-C_3N_4 composite, OMC dispersed and combined onto the surface of the g-C_3N_4. Thus, the clear interfaces between OMC and g-C_3N_4 was formed, which would facilitate the photogenerated electron transfer from the g-C_3N_4 to OMC. EDS analysis further revealed the presence of elements C and N in the OMC/g-C_3N_4 composite, indicating that SBA-15 was removed thoroughly. However, apart from the peaks ascribed to C and N elements, the peaks at 8-10 keV were observed in Figure 3D, which were resulted from the copper mesh support.

(Figure 3)

The N_2 adsorption-desorption isotherms of pure g-C_3N_4, pristine OMC and a series of OMC/g-C_3N_4 composites were shown in Figure 4A. Pure g-C_3N_4 showed no hysteresis loop, indicative of no pores existed in the sample. The pristine OMC and all the OMC/g-C_3N_4 composites exhibited type IV isotherms, which were characteristic of existed mesoporous materials. Correspondingly, the BJH pore size distributions of

the OMC/g-C_3N_4 composites in Figure 4B were among 3-5 nm, which was almost consistent with that of pristine OMC, further indicating the existence of mesopores. The BET surface area and pore volume of various samples were summarized in Table 2. The OMC/g-C_3N_4 composites possessed larger specific surface areas than pure g-C_3N_4, which was due to the presence of OMC with extremely high surface area. Moreover, the specific surface area of the composites increased with the contents of OMC increasing, which was beneficial to improve the photocatalytic activity of the composites.

(Table 2)

(Figure 4)

DRS was employed to characterize the optical absorption property of the OMC/g-C_3N_4 composites. In Figure 5, the pure g-C_3N_4 showed absorption from the UV light to visible light, and its band gap absorption edge was around 460 nm, corresponding to the band gap at 2.7 eV. The OMC/g-C_3N_4 displayed almost the same absorption edge as the pure g-C_3N_4, indicating that the OMC was not incorporated to the lattice of the g-C_3N_4, and it was only immobilized on the surface of the g-C_3N_4. [41] However, compared with pure g-C_3N_4, OMC/g-C_3N_4 composites exhibited increased absorption intensity in the 400-800 nm range, which suggested that OMC/g-C_3N_4 could absorb more energy of visible-light. In addition, the absorption intensity of the OMC/g-C_3N_4 composites improved obviously with the OMC content increasing, which was in agreement with the color change of sample from yellow to black, consistent with the previous reports. [36, 38] The optical results suggested that the OMC/g-C_3N_4 photocatalyst was more strongly responsive to the visible light than the

pristine g-C_3N_4, and might favor in enhancing the visible light catalytic activity.

(Figure 5)

Since photoluminescence spectrum emission arises from the recombination of excited electrons and holes, thus, PL technique is useful for disclosing the migration, transfer, and recombination processes of the photogenerated electron-hole pairs in the semiconductors. Figure 6 showed the PL spectra of pure g-C_3N_4 and OMC/g-C_3N_4 composites with the excitation wavelength of 325 nm. Apparently, pure g-C_3N_4 exhibited the enhanced intensity of emission spectrum, however, in the OMC/g-C_3N_4 composites, the intensities were remarkably reduced with the amounts of OMC increasing. As we known, a weaker PL intensity represents a lower recombination probability of the electron-hole under light irradiation. Therefore, a certain amount of loaded OMC could significantly improve the photogenerated electrons and holes separation efficiency, leading to the enhancement in light utilization and photocatalytic efficiency.

(Figure 6)

To study the photocatalytic ability of as-prepared OMC/g-C_3N_4 composites, the RhB molecule was used as the model organic pollutant for the photodegradation reaction. Figure 7B showed the photocatalytic activities of pure g-C_3N_4 and a series of OMC/g-C_3N_4 composites under visible light irradiation. Without any catalyst photodegradation of RhB hardly carried out, which suggested that photoinduced self-sensitized photolysis of RhB could be neglected. When pure g-C_3N_4 catalyst was added, RhB concentration gradually decreased and the degradation efficiency was

23.6% for 60 min. Compared with pure g-C_3N_4, the OMC/g-C_3N_4 composites exhibited enhanced photocatalytic activities, the degradation efficiencies were at least 75.3% under the same conditions. The degradation activity improved with higher OMC content, in that the activity of OMC/g-C_3N_4-2 was higher than OMC/g-C_3N_4-1. However, a decrease in the activity was caused with further increase of OMC in OMC/g-C_3N_4-3, suggesting that the OMC content was important for the optimal photocatalytic activity. OMC/g-C_3N_4-2 composite exhibited the highest photocatalytic activity, almost 100.0% RhB was photodegraded with 60 min. Noticeably, the OMC modified g-C_3N_4 remarkably improved the absorption capability for organic dye, which could enrich more dye molecules on the surface of photoactive g-C_3N_4 particles, thus leading to accelerating the rates of photocatalytic reactions. As verified in Figure 7A, adsorption equilibrium was reached within 60 min for all the materials in dark, and the adsorbed amounts of RhB were 2.1% for g-C_3N_4, 12.1% for OMC/g-C_3N_4-1, 33.3% for OMC/g-C_3N_4-2 and 50.5% for OMC/g-C_3N_4-3, respectively. After the adsorption equilibrium, the reaction system was irradiated by visible light to perform the photocatalytic process. As we know, the photocatalytic degradation process occurred on the surface of the photocatalyst, thus the catalyst with higher surface area adsorbed more organic pollutants, which tended to display higher activity. However, the enhancements in the opacity and light scattering at higher OMC contents resulted in the reduction of light passing through the reaction suspension solution, the above two opposite reasons caused the highest degradation activity on OMC/g-C_3N_4-2. Figure 7C illustrated the variations in optical absorption spectra of RhB dye with

irradiation time over OMC/g-C_3N_4-2. The obviously reduced absorption intensity indicated that RhB degraded completely after 60 min irradiation. A linear relationship between ln (C_0/C) and the irradiation time was shown in Figure 7D. The linear relationships ($R \geq 0.99$) suggested that the photocatalytic degradation curves in all cases fit well with pseudo-first-order kinetics. Correspondingly, compared with pure g-C_3N_4, the degradation rate constants of various OMC/g-C_3N_4 composites were enhanced significantly in Figure 7E. Especially, OMC/g-C_3N_4-2 exhibited the highest rate constant at 0.0534 min^{-1}, which was approximate 10 times larger than 0.00525 min^{-1} on pure g-C_3N_4.

(Figure 7)

It was obvious that the OMC/g-C_3N_4 composites exhibited improved photocatalytic activities due to the existence of OMC. And the positive effects of the OMC deposition came from the possible combined reasons. Firstly, OMC/g-C_3N_4 exhibited stronger absorption of visible light than g-C_3N_4. Generally, the photocatalyst absorbs more light, which means that it can utilize more energy of the light and tends to possess higher photocatalytic ability. [36, 38] Secondly, OMC/g-C_3N_4 possessed larger specific surface area than g-C_3N_4. Increased specific surface area increased adsorption capacity for the dye and could supply more active sites, leading to acceleration in photocatalysis rates. Thirdly, OMC/g-C_3N_4 composite had effective interfacial contact between OMC and g-C_3N_4. The loaded OMC could efficiently facilitate the photogenerated electron transfer from g-C_3N_4 to OMC, thus reducing the photogenerated electron-hole recombination rates greatly. As a result, the addition of

OMC could significantly enhance the photocatalytic activity of the OMC/g-C_3N_4 composite.

The stability of a photocatalyst is important for the practical applications. Hence, the photocatalytic degradation experiments of RhB over OMC/g-C_3N_4-2 were repeated up to five times under the same conditions and the results were shown in Figure 8. It was evident that the photodegradation activity did not change markedly after five recycles, which confirmed that OMC/g-C_3N_4-2 was not photocorroded during the photodegradation process and kept good stability.

(Figure 8)

In addition, the catalyst structure was further measured after the five photodegradation runs by XRD and FTIR. Figure 9A showed XRD patterns of OMC/g-C_3N_4-2 before and after the repeated photocatalytic reactions. The XRD pattern of the reused OMC/g-C_3N_4-2 was similar to that of the fresh catalyst, meaning that the OMC/g-C_3N_4 composite was stable during the photoreaction process. However, the used OMC/g-C_3N_4-2 showed the broader and lower diffraction intensities, which was resulted from the narrowed interplanar distance and/or interlayer stacking distance of OMC/g-C_3N_4-2 after the repeated runs. Similarly, as seen from Figure 9B, the FTIR of OMC/g-C_3N_4-2 after photodegradation were almost the same as the fresh catalyst, further proving the stability of the composite catalyst.

(Figure 9)

In the photodegradation process, some active species, such as hydroxyl radicals (•OH), superoxide radicals ($\bullet O_2^-$), electrons (e^-) and holes (h^+), were formed by light

irradiation. Generally, $\bullet O_2^-$ was obtained by direct reduction of O_2 with electron ($e^- + O_2 \rightarrow \bullet O_2^-$). The •OH was generated by the direct hole oxidation or photogenerated electron induced multistep reductions of $\bullet O_2^-$ ($h^+ + H_2O \rightarrow \bullet OH + H^+$, $\bullet O_2^- + H^+ \rightarrow \bullet OOH$, $\bullet OOH + H^+ + e^- \rightarrow H_2O_2$, $H_2O_2 + e^- \rightarrow \bullet OH + OH^-$). In addition, h^+ could directly react with organic compounds if the photocatalyst has moderate redox potential. In order to detect the main reactive species for the degradation RhB over OMC/g-C_3N_4 and discuss the reaction mechanism, the control experiments of quenching active species were carried out. Herein, methanol was used to quench the •OH, [42, 43] p-benzoquinone (p-BQ) as $\bullet O_2^-$ scavenger, [43, 44] dimethyl sulfoxide (DMSO) as e^- scavenger, [45, 46] and ammonium oxalate (AO) as h^+ scavenger. [47] Figure 10 displayed the effects of different scavengers on the degradation activities. The additions of methanol and DMSO had medium effects on the activities, which implied that •OH and e^- were reactive but not the main active species. However, it was interesting to find that when AO was added, the degradation efficiency was evidently improved, indicating that photogenerated holes were not the main active species, either. The possible reasons of acceleration in activity with AO adding were that AO as h^+ scavenger not only depressed the reaction, at the same time, it could effectively accelerate the photogenerated electron-hole pairs separation, which was observed in the previous study. [48] Moreover, the degradation efficiency of RhB was decreased to 51.8% with the addition of p-BQ, which suggested that $\bullet O_2^-$ was the main reactive species.

(Figure 10)

Based on the detection of active species in the photodegradation process and characterizations of photocatalyst, a clear synergetic effect between OMC and photoactive g-C_3N_4 for the enhancement in the activity was proposed. First, OMC showed great adsorption capacity to dye, which was beneficial to the improved concentration of dye on the photoactive g-C_3N_4. Then OMC/g-C_3N_4 was irradiated and absorbed more energy of visible light. Electrons (e^-) in the conduction band (CB) and the same amounts of holes (h^+) in the valence band (VB) were excited (Eq. 1). Moreover, the interfacial contact formed between the OMC and g-C_3N_4 could effectively facilitate the electrons transfer from the photoactive g-C_3N_4 to OMC and effectively collected by OMC, thus the recombination rates of the electron-hole pairs were hindered to achieve the effective charge separation. And correspondingly, the abundant holes were left on the valence band of g-C_3N_4. Then e^- was trapped by O_2 adsorbed on the surface of the catalyst to produce superoxide radical $\bullet O_2^-$ and $\bullet O_2^-$ radicals combined with H_2O to further transformed to active species •OH (Eqs. 2-5). According to scavenging experiments, photogenerated holes did not act as the active species. Hence, in OMC/g-C_3N_4 composite, h^+ did not react with RhB. And the generated active species such as e^-, $\bullet O_2^-$ and •OH reacted with the organic dye to generate the degradation products (Eq. 6). The significant enhancements in photocatalytic activity on OMC/g-C_3N_4 composite was resulted from the combined factors including the enhanced visible light adsorption, enriched adsorption of dye on the photocatalyst and subsequent efficient separation of photogenerated electrons and holes. The possible reaction process was proposed as the followings:

$$OMC/g\text{-}C_3N_4 + \text{visible light} \rightarrow e^- + h^+ \quad (1)$$

$$e^- + O_2 \rightarrow \bullet O_2^- \quad (2)$$

$$\bullet O_2^- + H^+ \rightarrow \bullet OOH \quad (3)$$

$$\bullet OOH + H^+ + e^- \rightarrow H_2O_2 \quad (4)$$

$$H_2O_2 + e^- \rightarrow \bullet OH + OH^- \quad (5)$$

$$\bullet OH, \bullet O_2^-, e^- + RhB \rightarrow \text{degradation products} \quad (6)$$

(Figure 11)

4. Conclusions

The novel visible-light-driven OMC/g-C_3N_4 photocatalyst was synthesized by a facile heating method. The properties of OMC/g-C_3N_4 composites, such as optical, catalytic properties and the absorption capacity were improved by introduction of the ordered mesoporous carbon. The enhanced photocatalytic performance was attributed to the synergetic effects between g-C_3N_4 and OMC. The introduced OMC has been found to have multiple functions, including increasing visible light absorption, enhancing the enrichment of dye concentration on the photoactive centers and facilitating the separation of photogenerated electron-hole pairs. Moreover, the coupled photocatalyst with g-C_3N_4 and OMC possessed good stability without significant loss in activity after five repeated runs. Therefore, OMC/g-C_3N_4 composite may be a promising efficient photocatalyst for degradation of organic pollutants.

Acknowledgement

We sincerely acknowledge the financial supports from National Natural Science Foundation of China (21073049, 21373069), New Century Excellent Talents in University (NCET-10-0064), State Key Lab of Urban Water Resource and Environment of Harbin Institute of Technology (HIT2013TS01) and the Fundamental Research Funds for the Central Universities (HIT. IBRSEM. 201327).

References

1. I. K. Konstantinou and T. A. Albanis, Appl. Catal. B: Environ., 2004, **49**, 1-14.
2. A. Kumar, A. S. Patel and T. Mohanty, J. Phys. Chem. C, 2012, **116**, 20404−20408.
3. Y. Dong, K. He, L. Yin and A. Zhang, Nanotechnology, 2007, **18**, 435602–435607.
4. W. Jiao, L. Wang, G. Liu, G. Q. Lu and H. M. Cheng, ACS Catal., 2012, **2**, 1854−1859.
5. E. S. Jang, J. H. Won, S. J. Hwang and J. H. Choy, Adv. Mater., 2006, **18**, 3309-3312.
6. L. Li, L. Xu, W. Shi and J. Guan, Int. J. Hydrogen Energy, 2013, **38**, 816−822.
7. A. Fujishima and K. Honda, Nature, 1972, **238**, 37−38.
8. J. G. Yu, G. P. Dai, Q. J. Xiang and M. Jaroniec, J. Mater. Chem., 2011, **21**, 1049−1057.
9. J. Matos, M. Hofman and R. Pietrzak, Carbon, 2013, **54**, 460−471.
10. D. Wang, L. Xiao, Q. Luo, X. Li, J. An and Y. Duan, J. Hazard. Mater., 2011, **192**,

150−159.

11. B. Kiskan, J. Zhang, X. Wang, M. Antonietti and Y. Yagci, ACS Macro. Lett., 2012, **1**, 546−549.
12. Y. Gong, P. Zhang, X. Xu, Y. Li, H. Li and Y. Wang, J. Catal., 2013, **297**, 272−280.
13. C. Pan, J. Xu, Y. Wang, D. Li and Y. Zhu, Adv. Funct. Mater., 2012, **22**, 1518−1524.
14. X. C. Wang, K. Maeda, A. Thomas, K. Takanabe, G. Xin, J. M. Carlsson, K. Domenet and M. Antonietti, Nat. Mater., 2009, **8**, 76−80.
15. A. B. Jorge, D. J. Martin, M. T. S. Dhanoa, A. S. Rahman, N. Makwana, J. Tang, A. Sella, F. Cora, S. Firth, J. A. Darr and P. F. McMillan, J. Phys. Chem. C, 2013, **117**, 7178−7185
16. H. Yan, Y. Chen and S. Xu, Int. J. Hydrogen Energy, 2012, **37**, 125−133.
17. X. C. Wang, K. Maeda, X. F. Chen, K. Takanabe, K. Domen, Y. D. Hou, X. Z. Fu and M. Antonietti, J. Am. Chem. Soc., 2009, **131**, 1680−1681.
18. J. Zhang, F. Guo and X. Wang, Adv. Funct. Mater., 2013, **23**, 3008−3014.
19. S. C. Yan, Z. S. Li and Z. G. Zou, Langmuir, 2009, **25**, 10397−10401.
20. L. Huang, H. Xu, Y. Li, H. Li, X. Cheng, J. Xia, Y. Xu and G. Cai, Dalton Trans., 2013, **42**, 8606–8616.
21. S. Ye, L. G. Qiu, Y. P. Yuan, Y. J. Zhu, J. Xia and J. F. Zhu, J. Mater. Chem. A, 2013, **1**, 3008−3015.
22. J. X. Sun, Y. P. Yuan, L. G. Qiu, X. Jiang, A. J. Xie, Y. H. Shen and J. F. Zhu

Dalton Trans., 2012, **41**, 6756–6763.

23. J. Xu, Y. Wang and Y. Zhu, Langmuir, 2013, **29**, 10566−10572.
24. S. C. Lee, H. O. Lintang and L. Yuliati, Chem. Asian J., 2012, **7**, 2139−2144.
25. F. Dong, L. Wu, Y. Sun, M. Fu, Z. Wu and S. C. Lee, J. Mater. Chem., 2011, **21**, 15171−15174.
26. G. Liu, P. Niu, C. H. Sun, S. C. Smith, Z. G. Chen, G. Q. Lu and H. M. Cheng, J. Am. Chem. Soc., 2010, **132**, 11642−11648.
27. N. Cheng, J. Tian, Q. Liu, C. Ge, A. H. Qusti, A. M. Asiri, A. O. Al-Youbi and X. Sun, ACS Appl. Mater. Interfaces, 2013, **5**, 6815−6819.
28. L. Ge, C. C. Han and J. Liu, J. Mater. Chem., 2012, **22**, 11843−11850.
29. J. Fu, B. Chang, Y. Tian, F. Xi and X. Dong, J. Mater. Chem. A, 2013, **1**, 3083−3090.
30. S. Min and G. Lu, J. Phys. Chem. C, 2012, **116**, 19644−19652.
31. Y. Xu, H. Xu, J. Yan, H. Li, L. Huang, Q. Zhang, C. Huang and H. Wan, Phys. Chem. Chem. Phys., 2013, **15**, 5821−5830.
32. W. Wei, C. Yu, Q. Zhao, G. Li and Y. Wan, Chem. Eur. J., 2013, **19**, 566−577.
33. Q. P. Luo, X. Y. Yu, B. X. Lei, H. Y. Chen, D. B. Kuang and C. Y. Su, J. Phys. Chem. C, 2012, **116**, 8111−8117.
34. P. Dong, Y. Wang, B. Cao, S. Xin, L. Guo, J. Zhang and F. Li, Appl. Catal. B: Environ., 2013, **132−133**, 45−53.
35. H. Zhang, X. Fan, X. Quan, S. Chen and H. Yu, Environ. Sci. Technol., 2011, **45**, 5731–5736.

36. Q. Xiang, J. Yu and M. Jaroniec, J. Phys. Chem. C, 2011, **115**, 7355–7363.

37. L. Ge and C. Han, Appl. Catal. B: Environ., 2012, **117–118**, 268–274.

38. G. Liao, S. Chen, X. Quan, H. Yu and H. Zhao, J. Mater. Chem., 2012, **22**, 2721–2726.

39. D. Zhao, Q. Huo, J. Feng, B. F. Chmelka and G. D. Stucky, J. Am. Chem. Soc., 1998, **120**, 6024−6036.

40. Y. Zhao, Z. Liu, W. Chu, L. Song, Z. Zhang, D. Yu, Y. Tian, S. Xie and L. Sun, Adv. Mater., 2008, **20**, 1777−1781.

41. Y. J. Wang, R. Shi, J. Lin and Y. F. Zhu, Energy Environ. Sci., 2011, **4**, 2922−2929.

42. L. Shi, L. Liang, J. Ma and J. M. Sun, Superlattice. Microst., 2013, **62**, 128−139.

43. R. Dong, B. Tian, J. Zhang, T. Wang, Q. Tao, S. Bao, F. Yang and C. Zeng, Catal. Commun., 2013, **38**, 16−20.

44. M. Yin, Z. Li, J. Kou and Z. Zou, Environ. Sci. Technol., 2009, **43**, 8361–8366.

45. D. Wang, Y. Duan, Q. Luo, X. Li, J. An, L. Bao and L. Shi, J. Mater. Chem., 2012, **22**, 4847−4854.

46. L. Shi, L. Liang, J. Ma, Y. Meng, S. Zhong, F. Wang and J. M. Sun, Ceram. Int., 2014, **40**, 3495–3502.

47. S. Kumar, T. Surendar, A. Baruah and V. Shanker, J. Mater. Chem. A, 2013, **1**, 5333−5340.

48. Y. Tian, B. Chang, J. Lu, J. Fu, F. Xi and X. Dong, ACS Appl. Mater. Interfaces, 2013, **5**, 7079−7085.

Table 1 Elements contents in various samples

Sample	C/wt%	N/wt%	C/N atomic ratio
g-C_3N_4	34.45	62.02	0.65
OMC/g-C_3N_4-1	34.62	59.02	0.68
OMC/g-C_3N_4-2	36.48	57.36	0.74
OMC/g-C_3N_4-3	37.73	55.84	0.79

Table 2 BET surface area and pore volume of various samples

Samples	BET surface area (m^2/g)	Pore volume (cm^3/g)
g-C_3N_4	2.41	0.023
OMC/g-C_3N_4-1	15.84	0.062
OMC/g-C_3N_4-2	30.13	0.116
OMC/g-C_3N_4-3	43.76	0.096
OMC	1120.48	1.250

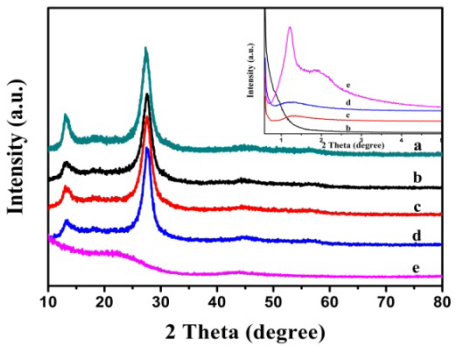

Figure 1. XRD patterns of (a) pure g-C_3N_4, (b) OMC/g-C_3N_4-1, (c) OMC/g-C_3N_4-2, (d) OMC/g-C_3N_4-3, and (e) OMC. Inset is SAXRD patterns.

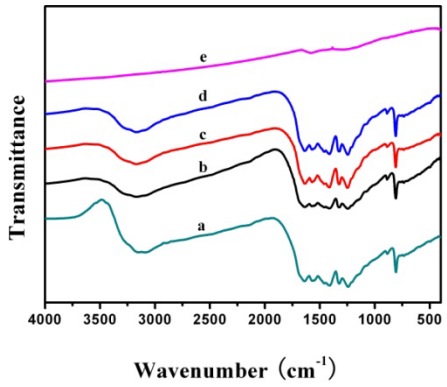

Figure 2. FTIR spectra of (a) pure g-C_3N_4, (b) OMC/g-C_3N_4-1, (c) OMC/g-C_3N_4-2, (d) OMC/g-C_3N_4-3, and (e) OMC.

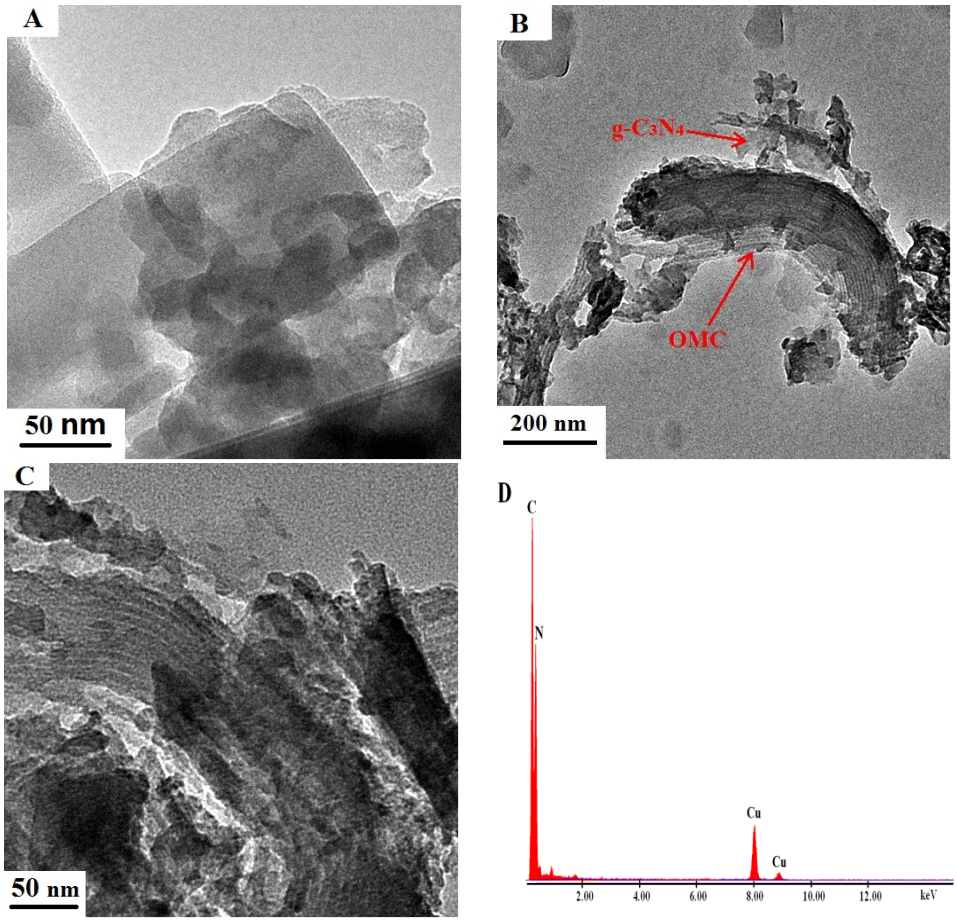

Figure 3. TEM images of (A) pure g-C_3N_4, (B, C) OMC/g-C_3N_4-2 and (D) EDS analysis for OMC/g-C_3N_4-2 composite.

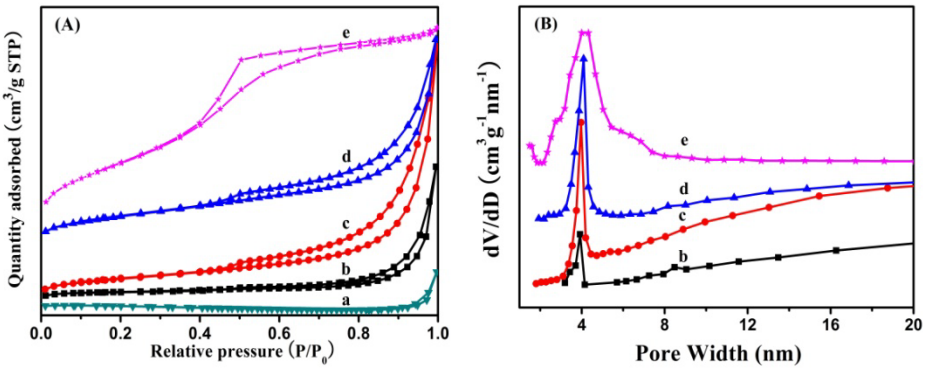

Figure 4. (A) N_2 adsorption-desorption isotherms and (B) Pore size distributions of (a) pure g-C_3N_4, (b) OMC/g-C_3N_4-1, (c) OMC/g-C_3N_4-2, (d) OMC/g-C_3N_4-3, and (e) OMC.

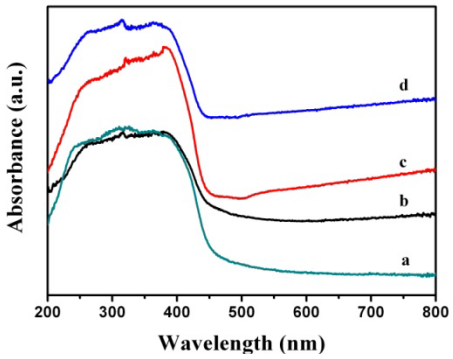

Figure 5. UV-vis diffuse absorption spectra of (a) pure g-C_3N, (b) OMC/g-C_3N_4-1, (c) OMC/g-C_3N_4-2, and (d) OMC/g-C_3N_4-3.

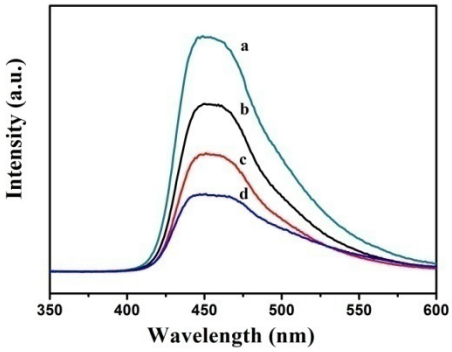

Figure 6. Photoluminescence emission spectra of (a) pure g-C_3N_4, (b) OMC/g-C_3N_4-1, (c) OMC/g-C_3N_4-2 and (d) OMC/g-C_3N_4-3.

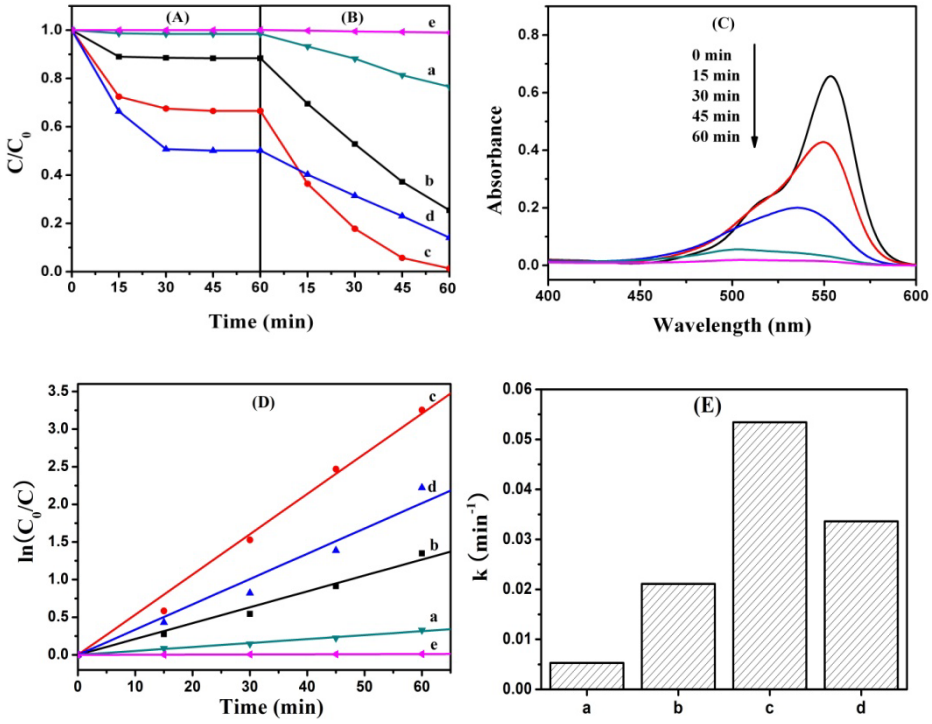

Figure 7. (A) The adsorption curves of RhB; (B) Photodegradation of RhB; (C) UV-vis absorption spectra of RhB over OMC/g-C_3N_4-2 composite for different irradiation times; (D) First-order kinetic plots for the photodegradation of RhB; (E) The rate constants of (a) pure g-C_3N_4, (b) OMC/g-C_3N_4-1, (c) OMC/g-C_3N_4-2, (d) OMC/g-C_3N_4-3, and (e) without catalyst.

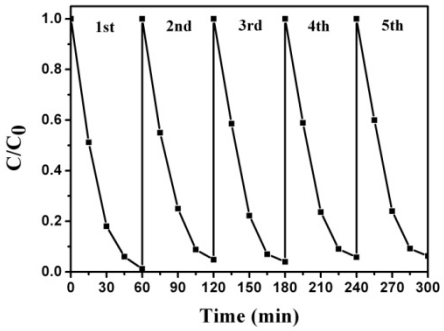

Figure 8. Recycling runs in the photodegradation of RhB over OMC/g-C_3N_4-2.

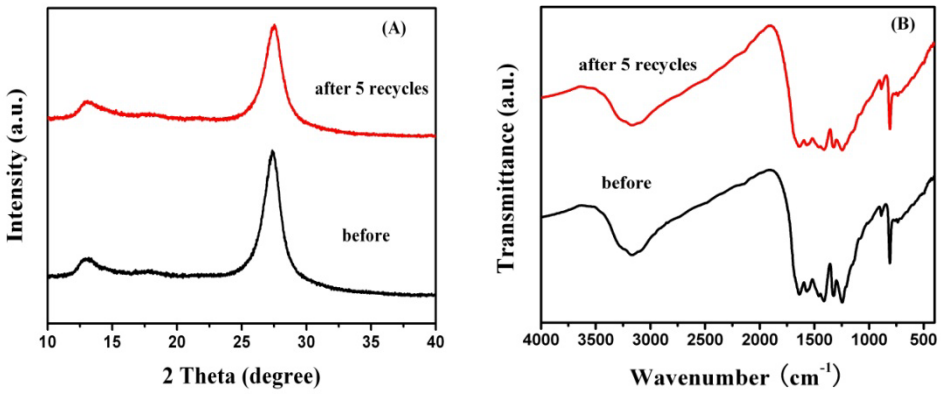

Figure 9. (A) XRD patterns and (B) FTIR of OMC/g-C_3N_4-2 before and after five recycling reactions.

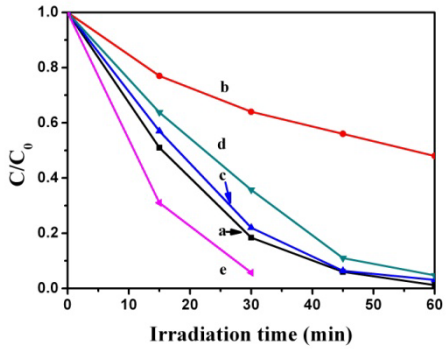

Figure 10. Effects of different active scavengers on the degradation RhB over OMC/g-C_3N_4-2: (a) no scavenger, (b) adding p-benzoquinone, (c) adding methanol, (d) adding DMSO, and (e) adding ammonium oxalate.

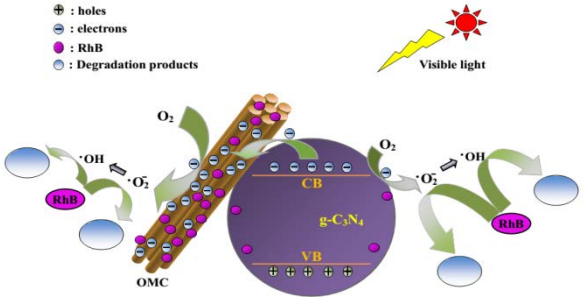

Figure 11. The proposed photodegradation process on OMC/g-C_3N_4 composite.

Graphic abstract

Due to the loaded OMC, photogenerated electrons and holes were efficiently separated, which made OMC/g-C_3N_4 exhibit enhanced visible light activity.